

# Mitigated blistering and deuterium retention in tungsten exposed to high-flux deuterium-neon mixed plasmas

L Cheng<sup>1,2</sup>, G De Temmerman<sup>3</sup>, T W Morgan<sup>4</sup>, T. Schwarz-Selinger<sup>5</sup>, Y. Yuan<sup>1,2</sup>, H.B. Zhou<sup>1,2</sup>, B Wang<sup>6</sup>, Y Zhang<sup>1,2</sup> and G H Lu<sup>1,2\*</sup>

<sup>1</sup> School of Physics and Nuclear Energy Engineering, Beihang University, Beijing 100191, China

<sup>2</sup> Beijing Key Laboratory of Advanced Nuclear Materials and Physics, Beihang University, Beijing 100191, China

<sup>3</sup> ITER Organization, Route de Vinon sur Verdon, CS90 046, 13067 St Paul Lez Durance Cedex, France

<sup>4</sup> FOM Institute DIFFER, Dutch Institute for Fundamental Energy Research, Association EURATOM-FOM, Trilateral Euregio Cluster, Eindhoven, the Netherlands

<sup>5</sup> Max-Planck-Institut für Plasmaphysik, EURATOM Association, Boltzmannstr. 2, D-85748 Garching, Germany

<sup>6</sup> College of Materials Science and Engineering, Beijing University of Technology, Beijing, China

Email: LGH@buaa.edu.cn

**Abstract.** Surface morphology and deuterium retention in tungsten exposed at surface temperature of  $\sim 550$  K to mixed deuterium-neon plasmas of different neon concentrations are investigated. It is found that the addition of neon up to 20% mitigates blistering on the surface. Cross-section view of the surface shows the formation of pores near the surface in the depth less than 100 nm. Deuterium depth profile is featured by an enhanced deuterium concentration within a depth of 16 nm but a mitigated penetration in depth larger than 1  $\mu\text{m}$ . Deuterium retention is reduced by up to a factor of four. It is suggested the open pores formed in the surface serves as an escaping channel, mitigates deuterium penetration towards bulk and retention in the bulk.

Keywords: deuterium retention, neon, tungsten, plasma-material interaction

PACS: 52.40.Hf

## 1. Introduction

Tungsten is considered as one of the promising plasma facing materials for future fusion devices due to its high melting point and thermal conductivity as well as the low erosion rate and hydrogen inventory [1]. Indeed a full tungsten divertor will be used in ITER from the beginning of operation [2]. Reduction of the heat fluxes to the divertor surfaces is typically achieved by radiative cooling through the injection of extrinsic impurities such as nitrogen or inert gases (neon and argon) in the divertor [3–5]. However, the presence of those seeded impurities in the plasma will alter the interaction between the plasma and the plasma facing components, such as the surface morphology evolution and hydrogen isotope diffusion and trapping [6]. Experiments in linear plasma devices have shown that deuterium trapping is reduced by helium [7–9] or increased by argon [10].

In this paper, we investigate the effect of inert gas neon addition in a high flux deuterium plasma on tungsten surface morphology changes and deuterium retention. Three neon concentrations, 5%, 10% and 20%, in mixed plasmas were used in the experiment, among which the 5% case mimics the condition of the maximum neon ion fraction expected in the ITER divertor. Surface and sub-surface morphology features in scales ranging from hundred nm to  $\mu\text{m}$  will be described. The correlation between trapped deuterium profile and surface damage depth is given. Measurement of deuterium depth profile and deuterium desorption profile will also be shown.

## 2. Experiment

Polycrystalline rolled tungsten targets (>99.95 wt.% purity) with an average grain size of 2-5  $\mu\text{m}$  from Advanced Technology and Materials Co., Ltd China were used in this experiment. Tungsten grains were elongated along the target surface during the rolling process, which is different from tungsten to be used in ITER (elongated grains are perpendicular to the target surface). Tungsten targets were mechanically polished to a mirror-like finish then annealed at 1273 K for one hour at

a background pressure of  $5 \times 10^{-4}$  Pa. The target is of a top-hat shape with a front surface of  $10 \times 15$  mm<sup>2</sup> and a surface of  $15 \times 15$  mm<sup>2</sup> in the bottom. The target thickness is 5.5 mm. The top-hat shape allows the target surface to be 1.4 mm higher than the top of the tungsten clamping ring which is used to maintain the sample on the cooled target holder, which avoids any pollution or deposition from the clamping ring.

### *2.1. Deuterium-neon mixed plasma exposure*

The W targets were exposed to mixed neon (Ne) and deuterium (D) plasmas in the linear plasma generator Pilot-PSI located at the FOM-Institute DIFFER [11]. The plasma is produced by a cascaded arc source and confined by an axial magnetic field of 0.4 T. In figure 1, the radial distribution of the electron density, electron temperature and surface temperature is shown. Electron density and temperature are measured by Thomson scattering (TS) at a distance of  $\sim 15$  mm from the surface. The pure deuterium plasma beam has a Gaussian profile with a peak electron density of  $\sim 2.0 \times 10^{20}$  m<sup>-3</sup> and a full width half maximum of  $\sim 11$  mm. The electron temperature profile is relatively flat and the mean electron temperature is  $\sim 1.1$  eV. Assuming that ions are accelerated to sonic speed at the sheath entrance (Bohm criterion [12]), and that the plasma density at the sheath entrance is half of that at the pre-sheath, the ion flux is calculated based on electron density and temperature measured by TS, which is  $\sim 1.2 \times 10^{24}$  m<sup>-2</sup>s<sup>-1</sup>. In case of D-Ne mixed plasmas, the peak electron density at the plasma center decreases while the electron temperature increases slightly. In the case of mixed species plasmas, the ion flux is estimated by considering the effective ion mass derived from the different ion concentrations with optical emission spectroscopy as described later. Irradiations with no Ne, 5% Ne, 10% Ne and 20% Ne ions in the mixed plasma are referred to as pure D, D-5Ne, D-10Ne and D-20Ne, respectively. The D fluence is fixed at  $\sim 3 \times 10^{26}$  m<sup>-2</sup> in all conditions. During plasma exposure, a negative bias of -40 V is applied to the target which results in an incident energy of  $\sim 40$  eV as the plasma potential is relatively small (a few V). The surface temperature profile with a spatial resolution of 0.33 mm on the target is measured by an

infrared camera (FLIR SC7500-MB) with the emissivity set to 0.05. The infrared camera is calibrated with a black body and the uncertainty of the measurement is about 10 K in the experiment. Details of calibration and measurement by the infrared camera can be found in [13]. Temperatures measured at the center and at the edge of each target are summarized in table 1.

## 2.2 Neon ion concentration measurement

The neon ion concentration is estimated by optical emission spectroscopy (OES) by utilizing the intensity ratio of Ne I line at 470.886 nm to D I line at 372.090 nm. This line intensity ratio is also measured using OES and calibrated using a residual gas analyzer (RGA) in Magnum-PSI [14], a linear plasma device generating similar plasmas as in Pilot-PSI with more diagnostics.

The OES measurements were performed at a distance of ~15 mm from the target surface in both Pilot-PSI and Magnum-PSI. The light is collected by a lens and coupled into an optical fiber. The fiber is led to an optical multichannel analyzer which consists of a Czerny-Turner spectrometer and a two-dimensional CCD camera. By means of an integrating sphere the optical system was absolutely calibrated.

Assuming deuterium and neon atoms in the upper states  $n$  are in partial localized thermodynamic equilibrium (PLTE), the population of atoms in excited levels can be derived from the Saha-Boltzmann equation:

$$\frac{n_e n_i}{n_n} = \frac{2g_i}{g_n a_0^3} \left( \frac{kT_e}{4\pi E_H} \right)^{3/2} \exp\left(-\frac{E_{ni}}{kT_e}\right), \quad (1)$$

where  $E_H$  is the ionization energy of the hydrogen atom,  $E_{ni} = E_\infty - E_n$  is the ionization energy of the particle in state  $n$ .  $g_n$  is the statistical weight of particle in state  $n$ . The statistical weight  $g_i$  of the ion is 2 for the ground state of  $\text{Ne}^+$  and 1 for the ground state of  $\text{D}^+$ .

The population densities of the excited levels are calculated from the measured intensities

$$I_{nm} = \frac{hc}{4\pi\lambda} A_{nm} n_n. \quad (2)$$

The Einstein coefficients  $A_{nm}$  is taken from [15] for neon and [16] for deuterium. Thus the ratio of the deuterium ion density  $n_i^D$  to the singly ionized neon ion density  $n_i^{Ne}$  is given using a combination of the Saha–Boltzmann equations (1) for deuterium and neon. Neon ion in higher charge states are not considered as the electron temperature is quite low (<3 eV). Then the ratio of the ion densities is given by the ratio of the atom densities corrected by the statistical weights as follows:

$$\frac{n_i^{Ne}}{n_i^D} = \frac{n_n^{Ne}}{n_n^D} \cdot \frac{g_i^{Ne}/g_n^{Ne}}{g_i^D/g_n^D} \cdot \exp\left(-\frac{E_{ni}^{Ne} - E_{ni}^D}{kT_e}\right). \quad (3)$$

Assuming the quasi-neutrality condition,  $n_e = n_i^{Ne} + n_i^D$ , and using the electron density and temperature from Thomson scattering measurement, the ratio of  $n_i^{Ne}$  to  $n_e$  can be evaluated.

The ion ratio measurement using OES was compared to simultaneous measurements in Magnum-PSI using RGA. Magnum-PSI utilizes the same plasma source and Thomson scattering system as Pilot-PSI to generate plasma and measure plasma parameters. The unique ability of Magnum-PSI is the low background pressure and large beam diameter with the high ion flux capabilities of Pilot-PSI. The low background pressure is achieved by differential pumping, where the vacuum chamber is divided by a flow restriction (skimmer) into separate chambers that are individually pumped [17]. The schematic in figure 2 gives the differentially pumped vacuum system. The plasma source chamber and target chamber are individually pumped by a roots pump with a pumping capability of 20000 m<sup>3</sup> h<sup>-1</sup>. It has been shown that most neutrals from the plasma source are on the edge of the plasma expansion, resulting in an effective blockage of the neutral flow toward the next chamber by the skimmer [18]. The ionized particles are transported from the source to the target chamber, where they are neutralized at the target surface and contribute to the neutral gas load in the target chamber.

Though a small fraction of neutral may penetrate through the skimmer, the pressure in the chamber containing the target is mainly set by the recombination of the incoming ion flux on the target surface, which permits the assumption of  $A'^0 \approx A^+$ , in which  $A'^0$  is the flux of neutrals originating from the recombined ions and  $A^+$  is the ion flux striking onto the target. A RGA was mounted on a small port close to the target via a needle valve and differentially pumped by a turbo pump. Considering the neutral gas is in thermal equilibrium with the chamber wall, so that the particle flux reaching RGA port ( $A'_{TB}{}^0$ ) is proportional to that at the roots port ( $A'_{TB}{}^0 \propto A'^0 \approx A^+$ ). The RGA was working with turbo pump running. In the dynamic pumping system, the neutral flux measured by the RGA is given by,

$$\frac{dN}{dt} \approx n_0 \frac{V}{\tau} p - L, \quad (4)$$

in which  $N$  is the number of particles,  $p$  is the partial pressure of the detected gas,  $n_0$  is constant,  $V/\tau$  is the pumping speed (volume over a pumping time constant),  $L$  is background leak rate of the monitored gas. Considering the effect of mass discrimination of the needle valve and ionization of neutral at 70 eV electron impact in the RGA electron emitter, a correction factor is used. Then the flux ratio of two detected neutrals can be simply related to partial pressure monitored in the RGA, assuming a negligible background leak rate ( $L$ ). This is given by,

$$\frac{dN_{Ne}/dt}{dN_D/dt} = Const. \frac{p_{Ne}}{p_D}. \quad (5)$$

Plasma with electron densities of  $1.6-2.0 \times 10^{19} \text{ m}^{-3}$  and the electron temperature of 1.0-1.8 eV were measured at Magnum-PSI. The electron density was about one magnitude lower than that in Pilot-PSI but the electron temperature remains similar. Figure 3 shows the relationship between the neon fraction in the gas flow in the plasma source and the neon ion fraction measured by OES and RGA in Magnum-PSI and Pilot-PSI. The results indicate that even at 50% neon inlet gas flow, neon ion percentage less than 20% is found in the mixed plasma, which is partly attributed to the higher ionization energy of neon. It is seen that in conditions of gas flow ratio below 80%, results of OES

overestimate the neon ion concentration inside the plasma. For the exposure experiment at Pilot-PSI, the neon ion ratio measured using OES is corrected according to the relationship between neon ion and gas ratio found in Magnum-PSI.

## *2.2. Target analysis*

The surface morphology of the tungsten targets was studied by a scanning electron microscope (SEM, Zeiss SIGMA). The images were taken in the center of the plasma-exposed region by using typically a 10 kV electron beam in inlens mode. The sub-surface morphology was analyzed after cross-sectioning by a SEM combined with a focused ion beam (TESCAN LYRA3 FEG-SEM/FIB). For targets exposed to D-10Ne and D-20Ne, a Pt-C film was deposited onto the investigated surface in situ prior to the cross-sectioning to reduce artifacts caused by the Ga ion beams. The observation was made at a tilt angle of 55°.

The D depth profile in the W targets was determined by nuclear reaction analysis (NRA) at IPP, Garching [19,20]. The targets were probed by  $^3\text{He}$  beam with a spot of  $\sim 1$  mm diameter at four positions on the surface (indicated by vertical lines in figure 1) to extract a radial scan. By utilizing the  $\text{D}(^3\text{He}, \text{p})^4\text{He}$  reaction,  $^4\text{He}$  and proton spectra were measured with  $^3\text{He}$  ion beams of energies ranging from 0.5 to 4.5 MeV. NRADC [21] program was used to evaluate the NRA spectra and determine the D depth profile at depths up to 7  $\mu\text{m}$ . The uncertainty of the measurement is about 5%.

Deuterium desorption was analyzed by thermal desorption spectroscopy (TDS) at the FOM-Institute DIFFER. The target temperature was measured using an S-type thermocouple which was attached to the back of the target during heating. The target was heated up to 1373 K with a heating rate of 1 K/s. The residual gases such as  $\text{D}_2$  (mass 4), HD (mass 3), and Ne or  $\text{D}_2\text{O}$  (mass 20) were monitored by a quadrupole mass spectrometer (Balzers QMA 124). A calibration leak was used to

determine the absolute sensitivity of the mass 2 and 4 signals. The sensitivity for mass 3 is assumed to be the average of the sensitivities for masses 2 and 4. The D<sub>2</sub> (mass 4) signal calibration is performed in the following way: before every TDS measurement, the calibration leak is turned on for a while and a calibration factor is obtained by dividing the leak flow by the D<sub>2</sub> signal intensity; then by applying this calibration factor to the acquired D<sub>2</sub> signal during TDS, the calibration is achieved. When calculating the total D retention, D from HD and D<sub>2</sub> is taken into account. D from mass 20 (D<sub>2</sub>O) may also contribute to D retention but is neglected in the calculation because of its low intensity during TDS and difficulty in calibration. D from HD usually contributes to less than 10% in the total D retention. The uncertainty in the measurement is mainly attributed to calibration process, which is about 5% in the present setup.

### **3. Results**

#### *3.1. Surface morphology*

Figure 4 shows the surface morphology of the W targets exposed to pure D and mixed Ne-D plasmas. In the case of pure D exposure (figure 4(a)), the surface is covered by blisters with sizes ranging from hundred nanometers to a few micrometers in diameter. The number density of blister is about 0.21  $\mu\text{m}^{-2}$ . Micrometric blisters are mostly multilayered structures with irregular edges. As shown in the following section, they originate from sub-surface grain boundaries. Larger magnification images, as shown in the second row, show nano-structures on both the target surface and the top of the blisters. These structures are typically lamellae and triangular and have sizes of 10-40 nm. The nano-structures are mostly observed in the high flux exposure experiments [22–24] and their formation is supposed to be correlated with the creation of a high concentration of defects in the near-surface region [22].



Ne addition to the plasma significantly affects the observed morphology changes. The blister size decreases and large blisters with size larger than 1 micron are rarely observed. The blister number density is about  $0.72 \mu\text{m}^{-2}$  and  $0.54 \mu\text{m}^{-2}$  for D-5Ne and D-10Ne, respectively. The nano-structure in D-10Ne in figure 4(c) differs from that observed in the cases of pure D and D-5Ne, and features open pores with diameter less than 20 nm. This is more pronounced for the D-20Ne case shown in figure 4(d), in which blistering is not observed and only small pores with a mean diameter of 50 nm are present. The formation of open pores appears to be a synergic effect of D and Ne, because neither pure D irradiation shown in figure 4a nor pure Ne plasma irradiation shown in figure 5b and 5c leads to the formation of such structures. The surface morphology of W targets exposed to pure Ne plasma with an incident energy of 40 eV at 550 K and  $5.2 \times 10^{25} \text{ Ne/m}^2$  only shows a physical sputtering pattern without any pinholes as shown in figure 5(b) and (c), which is consistent with our previous results at lower Ne incident energy of 20 eV [25].

### *3.2 Sub-surface morphology*

Cross-section of the exposed target was prepared and observed in a FIB-combined SEM. The top surface before FIB cut and the cross-section of the corresponding region is shown in figure 6. In case of pure D irradiation as shown in figure 6(a), inter-granular cavities are observed below large blisters, which follow the sub-surface grain boundaries at a depth of  $\sim 1 \mu\text{m}$ . This grain boundary is considered as a weak joining position between two adjacent grains and serves as a trapping site for D [26]. The accumulation of D at the grain boundary leads to a pressure build-up which promotes the sub-sequent crack, cavity growth following the grain boundary and finally the appearance of a blister on the top surface. The blister from inter-granular cavities indicates an affected depth of up to a few micrometers due to D diffusion during the plasma irradiation. Blisters with sizes in the range of hundred nanometers originate from cracks located closer to the surface, at a depth less than 500 nm. The crack is an intra-granular cavity and does not follow any grain boundary. The presence of the intra-granular crack is also observed in [23] under similar high-flux

D plasma exposure conditions. Accumulation of deuterium at defects, either intrinsic or induced by the high-flux plasma exposure, can be responsible for the formation of this near surface crack, serving a similar role as the sub-surface grain boundary, and promote blistering on the top surface.

Increasing the Ne ratio in the plasma, the density of micrometer size blister decreases and blisters in the hundred nanometer size range with sub-surface intra-granular cavities dominate the surface as shown in figure 6(b) and (c). In case of high Ne concentrations (D-10Ne and D-20Ne), only few blisters are observed within a few hundred grains and a strongly modified layer is observed up to a depth of tens of nanometer in figure 6(c) and (d). Surface topology of D-20Ne is further characterized as observed in a tilted angle. Besides the open pores mentioned in the previous section, small protrusions with diameter less than 500 nm are observed, and surface roughness is increased compared to the other 3 cases. The sub-surface region contains a high density of small cavities extending to depth of  $\sim 50$  nm and  $\sim 100$  nm for D-10Ne and D-20Ne, respectively. Some of the cavities even reach the top surface thus creating open pores. The higher the Ne concentration in a D-Ne mixed plasmas, the more intense the modifications of the sub-surface region but the shallower the affected depth.

### *3.2. Deuterium depth profiling*

Figure 7 shows the results of NRA measurements performed at the center, and 1 mm, 3 mm and 6 mm away from the center of the plasma-exposed region. The depth profiles clearly show that D penetration is mitigated by the presence of Ne in the mixed plasma. The D concentration is highest close to the surface and decreases with increasing depth. The average concentration within a depth of 16 nm is about 1.8 at. % for pure D and 1.6 at. % for D-5Ne. A local maximum in the deuterium concentration is observed at a depth between 0.2-1.3  $\mu\text{m}$  for pure D and at depth between 0.1-0.6  $\mu\text{m}$  for D-5Ne, after which the concentration decreases. This agrees well with the cross-section results by FIB-SEM, and the depth at which cavities are observed as shown in figure 6(a) and (b). For the D-10Ne and D-20Ne cases, a higher D concentration is measured very close to the surface

roughly in the same region where the open pore structure is observed in figure 6(c) and (d). The local maximum in the deuterium concentration observed at depth between 0.1-1  $\mu\text{m}$  seen for the pure D and D-5Ne cases is not apparent anymore for the higher Ne fractions. This is in agreement with the cross-section observation that blisters are rarely observed at a depth larger than 0.1  $\mu\text{m}$ . Besides, deuterium concentration is about 0.06 at. % at a depth of  $\sim 7 \mu\text{m}$  for the pure D case, which means that at depth beyond the NRA detection limit of 7  $\mu\text{m}$  more deuterium may be retained. Deuterium concentration falls to 0.06 at. % at a depth of  $\sim 3.2 \mu\text{m}$  for D-5Ne and  $\sim 1.0 \mu\text{m}$  for D-10Ne and D-20Ne, suggesting a strong reduction in inward deuterium diffusion in the presence of Ne in the mixed plasma.

The D depth profile varies with distance from the plasma center. For pure D, much less D retains at 6 mm off-center due to the exposure to a lower flux and fluence plasma as shown in figure 1. For D-10Ne and D-20Ne, measurement performed at 6 mm off-center differs from that at other positions, but shows a similar pattern as in pure D, characterized by a profile of a maximum at  $\sim 0.02 \mu\text{m}$  and a local maximum at  $\sim 0.2 \mu\text{m}$ . This is probably the result of an inhomogeneous neon ion distribution within the plasma beam. Although the neon ion distribution was not directly measured in the experiment, its influence is reflected in the electron density profile. In figure 1, two local maximums are found at +2 and -2 mm off-center in the electron density profile. Considering the investigation of radial profile of argon (Ar) ions in a mixed Ar-H plasma generated by a cascaded arc source [27], this is probably the position where the neon ion density peaks. At the center of the plasma, the Ne ion is more likely lost due to charge exchange process between  $\text{Ne}^+$  and  $\text{D}_2$  molecule. Thus the position of maximum splits into two parts. At the edge position of 6 mm off-center, the Ne ion density is expected to be even lower due to the charge exchange reaction, thus its effect on D diffusion is weaker.

### *3.3. Deuterium desorption*

TDS measurements were performed to study deuterium trapping properties. Results are shown in figure 8 in which D<sub>2</sub> desorption signals are plotted. Most targets show two clear desorption peaks at ~580 K and ~820 K, with a small deviation towards lower temperature in D-10Ne. For D-5Ne both peak intensities decrease by ~20% compared to pure D. For D-10Ne and D-20Ne, the intensity of the 580 K peak decreases slightly while the intensity of the 820 K peak is reduced by a factor of ~6 compared to pure D.

The desorption peak at ~580 K is observed in previous studies on D desorption in W exposed to D plasmas fluence of  $\sim 1.0 \times 10^{26}$  [23,25] and  $\sim 0.8 \times 10^{27} \text{ m}^{-2}$  [23] at 530 K in Pilot-PSI. According to [23], the trapping site corresponding to the 580 K peak can be ascribed to D trapping at defects such as dislocations, grain boundaries and mono-vacancies. These defects are considered as intrinsic defects uniformly distributed in the commercial W targets and cannot be removed by annealing at 1273 K. The peak intensity at 820 K is larger than  $2.0 \times 10^{18} \text{ D}_2 \text{ m}^{-2}\text{s}^{-1}$  for pure D and D-5Ne in which blistering is pronounced and is less than  $0.5 \times 10^{18} \text{ D}_2 \text{ m}^{-2}\text{s}^{-1}$  for D-10Ne and D-20Ne in which less blistering is observed. This correlation suggests that the desorption peak at 820K is related to the plasma-induced damage.

The total D retention, considering contributions from both D<sub>2</sub> and HD is shown in the last column of table 1. The D retention decreases with increasing Ne fraction in the mixed plasma. The maximum reduction rate of D retention is found for D-20Ne and is about a factor of four. In all conditions the amount of HD contributes to less than 10% in the total D retention.

During the TDS experiments, the mass 20 signal (Ne or D<sub>2</sub>O) was also monitored. The desorption spectrum of the mass 20 signal is similar for targets exposed to pure D and mixed D-Ne plasmas as was observed in our previous study [25]. It is therefore not possible to study the trapping of Ne in W by TDS in this study.

#### **4. Discussion**

In this study, we have investigated blistering and deuterium retention in targets exposed to high flux pure D and mixed D-Ne plasmas in Pilot-PSI. Surface morphology and D depth profile shows that the presence of Ne in the plasma mitigates blistering originating from inter-granular cavities and D diffusion towards the bulk. In our previous research at Pilot-PSI [25], Ne pre-irradiation showed to no effect on blistering but induced a reduction in D retention at 523 K, for Ne and D fluence of  $1.0 \times 10^{26} \text{ m}^{-2}$ , and it was suggested that trapped Ne interrupts the D transport and reduces D retention. In D ion-driven permeation experiment of Ne or Ar impurities in W [28] at an incident energy of 1 keV, it is found that the steady state D permeation flux was reduced by 50%~70% with Ne ion fraction of 3.5% compared to the case of pure D. It is considered that both sputtering and precipitation effects induced by Ne accounted for the reduction in the near surface D concentration which resulted in a reduced permeation flux. In either way of Ne implantation, D transport was partly mitigated resulting in a reduced retention or permeation flux.

When considering the effect of Ne, it is natural to consider the effect of helium (He), which is also a noble gas and will be present in the divertor plasma (and therefore interact with tungsten) as the product of D-T fusion reactions or T decay process. The effect of He has been investigated in several experiments and shows strong effects on reduction in D retention and blistering. The effect of He on retention was recently reviewed by Baldwin [9]. At a low plasma flux of  $\sim 1 \times 10^{20} \text{ m}^{-2}\text{s}^{-1}$  a reduction in D retention and penetration was found with 10% He in D plasma exposure at surface temperature of 320~650 K in ITER grade W [29]. For plasma fluxes of  $\sim 1 \times 10^{22} \text{ m}^{-2}\text{s}^{-1}$ , irradiation with He ion fractions of up to 20% [7,9] lead to a reduction of D retention by a factor of  $\sim 4.5$  in rolled W at 420 K. D depth profile was measured by NRA in [30] and demonstrated a strong reduction in D penetration in re-crystallized W exposed to a D plasma with 5% He at surface temperature of 470~725 K. Blister formation was suppressed in targets exposed to D-He mixed plasmas and the surface morphology of which was comparably smooth as that of the unexposed ones [7,10,30]. Internal microstructure analysis by transmission electron microscope (TEM)

suggests presence of He bubbles of size ranging from a few nanometers to more than 10 nm [7]. The reduction of blistering and D retention due to He is ascribed to the ability of helium to reduce D penetration into bulk W. According to the He nano-bubbles formation in the near surface, it is proposed in [31] that He bubbles serves as a diffusion barrier for hydrogen into the bulk leading to the reduction of diffusivity of hydrogen. First principle calculation [32] reveals a strong attraction between H and a He-defect cluster in W which results in a strong H segregation towards He.

In terms of similarity between He and Ne, both of them are insoluble in W because of the large solution energy in W (6.07 eV for He [32], 11.55 eV for Ne [33]). The large solution energy is ascribed to the volume expansion of the W matrix with He/Ne interstitials atoms. One of the consequences of the volume expansion is the formation of a low electron-density region. H is stable in such region as well as in regions near vacancy and vacancy-like defects [34]. This implies that interstitial Ne/He generated during mixed plasma irradiation could act as a trapping site for D atoms and result in the enhancement of the D concentration in W in the near-surface region up to 100 nm as demonstrated in the NRA results of this study and in [35].

The main feature of D-Ne mixed irradiation differing from D-He mixed irradiation is the structure formed in the near-surface region. The mean range of 40 eV Ne in W is  $\sim 0.6$  nm [36]. Due to diffusion of Ne, the affected depth is deeper than the mean range, probably up to  $\sim 100$  nm as observed in the FIB-SEM cross-section images in our experiment. D atom accumulates around interstitial or trapped Ne atoms along the Ne diffusion path resulting in the subsequent formation of D bubbles. Meanwhile, the sputtering threshold of W by Ne is  $\sim 40$  eV [36] which means physical sputtering happens during the irradiation and explains the surface pattern observed in figure 5. In the D-Ne mixed condition, sputtering by Ne may result in local effects, such as the removal of a few W atoms on the cap above D bubbles located close to the top surface, and in the formation of the open pores observed in figure 6. While in case of D-He mixed irradiations, the He mean range in W is about 1.8~2.7 nm at an incident energy of 40~100 eV [36] and He bubbles form deeply in

W up to several tens nm[37]. The sputtering threshold of W by He is  $\sim 125$  eV [36]. Thus, in case of He it is expected that the precipitation effect such as He bubble formation is stronger than that in case of Ne and dominates the surface structure during D-He mixed irradiation.

Ne in mixed D-Ne irradiation is therefore considered to assist D accumulation. Considering the reduction of D penetration and total D retention, the mechanism proposed in [31] and [32] also works for the D-Ne case. The pore substitutes the role of He bubble in acting as a diffusion barrier for deuterium. On the one hand, pores connecting the top surface and sub-surface serve as escaping channels for D. On the other hand, the presence of pores increases the surface area leading to an increase in recombination and release of D molecule during irradiation.

In terms of H isotope inventory, impurity-seeding with Ne is considered to be beneficial. But it should be noted that this Ne effect is noticeable mainly for large fractions of Ne ( $>10\%$ ) in the plasma, which is not going to be the case in ITER (Ne ion fraction less than 5%). The pores formed during mixed D-Ne mixed plasma irradiation may have side effects on W divertor component operation. The presence of pores and high D concentration in the near surface may lead to a reduced thermal conductivity thus decreased resistance to thermal transient events. Moreover, the surface structure could easily be modified. Figure 9 shows the surface morphology of D-20Ne before and after FIB cutting by Ga ion. Without Pt-C protection, protrusions are removed and pinholes on the surface are largely expanded due to sputtering from the Ga ions. This is probably due to the high D concentration in the top surface and a rough surface where particles are impinging in angles rather than in the normal direction. This surface modification could increase the loss of W.

## **5. Conclusions**

In the present study, the effect of mixed D-Ne plasma irradiation at different Ne concentrations on surface morphology and D retention is investigated. In terms of surface morphology, blister formation originating both from inter- and intra-granular cavities is mitigated in the presence of Ne.

In D-10Ne and D-20Ne, nanostructure formation such as open pores near the surface at a depth less than 100 nm is observed. D depth profile measured by NRA analysis shows an enhanced D concentration within a depth of ~16 nm but a mitigated diffusion at depth larger than 1  $\mu\text{m}$ . D retention is reduced by up to a factor of four.

The open pores on the surface are considered to act as a D diffusion barrier, thereby decreasing D retention due to the mechanism proposed in mixed D-He plasma irradiation [31,32]. The formation of open pores is suggested as the result of the interaction between Ne, D and W on the surface.

The present results show a potential beneficial effect by applying impurity-seeding of Ne in terms of H isotope inventory. But in the ITER divertor condition this Ne effect may be over-shadowed by the effect of other impurities as He because of the high Ne ion fraction required for effects to be observed. And it is also important to consider potential side effects such as the presence of pores on the surface, which requires more investigations.

### **Acknowledgement**

This work was supported by National Magnetic Confinement Fusion Science Program of China under Grant 2013GB109003. G. H. Lu acknowledges the support from the China National Funds for Distinguished Young Scientists under Grant 51325103. The views and opinions expressed herein do not necessarily reflect those of the ITER Organization.

### **Reference**

- [1] Philipps V. 2011 *J. Nucl. Mater.* **415** S2–9
- [2] Al. R.A.P. et *55th APS Meet. Denver, CO, USA, Pap. WE1.00001*
- [3] Kallenbach A., Bernert M., Dux R., Casali L., Eich T., Giannone L., Herrmann A., McDermott R., Mlynek A., Müller H.W., Reimold F., Schweinzer J., Sertoli M., Tardini G., Treutterer W., Viezzer E., Wenninger R. and Wischmeier M. 2013 *Plasma Phys. Control. Fusion* **55** 124041
- [4] Rapp J., Monier-Garbet P., Matthews G., Sartori R., Andrew P., Dumortier P., Eich T., Fundamenski W., Hellermann M. von, Hogan J., Ingesson L., Jachmich S., Koslowski H., Loarte A., Maddison G., McDonald D., Messiaen A., Ongena J., Parail V., Philipps V., Saibene G., Unterberg B. and Contributors J.E. 2004 *Nucl. Fusion* **44** 312–9



- [5] Schweinzer J., Sips A.C.C., Tardini G., Schneider P.A., Fischer R., Fuchs J.C., Gruber O., Hobirk J., Kallenbach A., McDermott R.M., Neu R., Pütterich T., Rathgeber S.K., Stober J. and Vicente J. 2011 *Nucl. Fusion* **51** 113003
- [6] Kallenbach a., Balden M., Dux R., Eich T., Giroud C., Huber a., Maddison G.P., Mayer M., McCormick K., Neu R., Petrie T.W., Pütterich T., Rapp J., Reinke M.L., Schmid K., Schweinzer J. and Wolfe S. 2011 *J. Nucl. Mater.* **415** S19–26
- [7] Miyamoto M., Nishijima D., Ueda Y., Doerner R.P., Kurishita H., Baldwin M.J., Morito S., Ono K. and Hanna J. 2009 *Nucl. Fusion* **49** 65035
- [8] Ueda Y., Peng H.Y., Lee H.T., Ohno N., Kajita S., Yoshida N., Doerner R., De Temmerman G., Alimov V. and Wright G. 2013 *J. Nucl. Mater.* **442** S267–72
- [9] Baldwin M.J., Doerner R.P., Wampler W.R., Nishijima D., Lynch T. and Miyamoto M. 2011 *Nucl. Fusion* **51** 103021
- [10] Reinhart M., Kreter A., Buzi L., Rasinski M., Pospieszczyk A., Unterberg B. and Linsmeier C. 2014 *J. Nucl. Mater.*
- [11] De Temmerman G., Zielinski J.J., van Diepen S., Marot L. and Price M. 2011 *Nucl. Fusion* **51** 73008
- [12] Bohm D. 1949 *The Characteristics of Electrical Discharges in Magnetic Fields* ed A Guthrie and R K Wakerling (New York: McGraw-Hill)
- [13] van den Berg M. a., Bystrov K., Pasquet R., Zielinski J.J. and De Temmerman G. 2013 *J. Nucl. Mater.* **438** S431–4
- [14] De Temmerman G., van den Berg M. a., Scholten J., Lof a., van der Meiden H.J., van Eck H.J.N., Morgan T.W., de Kruijf T.M., Zeijlmans van Emmichoven P. a. and Zielinski J.J. 2013 *Fusion Eng. Des.* **88** 483–7
- [15] Wiese W.L. and Glennon B.M. 1966 *Atomic Transition Probabilities Volume I Hydrogen Through Neon, (NSRDS-NBS 4)* (Washington: US Govt. Printing Office)
- [16] Wiese W.L. and Fuhr J.R. 2009 *J. Phys. Chem. Ref. Data* **38** 565–719
- [17] van Eck H.J.N., Kleyn A.W., Lof A., van der Meiden H.J., van Rooij G.J., Scholten J. and Zeijlmans van Emmichoven P.A. 2012 *Appl. Phys. Lett.* **101** 224107
- [18] van Eck H.J.N., Hansen T. a R., Kleyn a W., van der Meiden H.J., Schram D.C. and Zeijlmans van Emmichoven P. a 2011 *Plasma Sources Sci. Technol.* **20** 45016
- [19] Alimov V.K., Mayer M. and Roth J. 2005 *Nucl. Instruments Methods Phys. Res. Sect. B Beam Interact. with Mater. Atoms* **234** 169–75
- [20] Mayer M., Gauthier E., Sugiyama K. and von Toussaint U. 2009 *Nucl. Instruments Methods Phys. Res. Sect. B Beam Interact. with Mater. Atoms* **267** 506–12
- [21] Schmid K. and Von Toussaint U. 2012 *Nucl. Instruments Methods Phys. Res. Sect. B Beam Interact. with Mater. Atoms* **281** 64–71
- [22] Xu H.Y., Luo G.N., Schut H., Yuan Y., Fu B.Q., Godfrey a., Liu W. and Temmerman G.D. 2014 *J. Nucl. Mater.* **447** 22–7
- [23] 't Hoen M.H.J., Balden M., Manhard a., Mayer M., Elgeti S., Kleyn a. W. and Zeijlmans van Emmichoven P. a. 2014 *Nucl. Fusion* **54** 83014

- [24] Jia Y.Z., Liu W., Xu B., Luo G.-N., Li C., Fu B.Q. and De Temmerman G. 2015 *J. Nucl. Mater.* **463** 312–5
- [25] Cheng L., De Temmerman G., Zeijlmans van Emmichoven P. a., Ji G., Zhou H.B., Wang B., Yuan Y., Zhang Y. and Lu G.H. 2015 *J. Nucl. Mater.* **463** 1025–8
- [26] Zhou H.-B., Liu Y.-L., Jin S., Zhang Y., Luo G.-N. and Lu G.-H. 2010 *Nucl. Fusion* **50** 25016
- [27] Meulenbroeks R.F.G. 1994 *Phys. Rev. E* **49**
- [28] Ishida M., Lee H.T. and Ueda Y. 2015 *J. Nucl. Mater.* **463** 1062–5
- [29] Ogorodnikova O. V., Schwarz-Selinger T., Sugiyama K. and Alimov V.K. 2011 *J. Appl. Phys.* **109** 13309
- [30] Alimov V.K., Shu W.M., Roth J., Sugiyama K., Lindig S., Balden M., Isobe K. and Yamanishi T. 2009 *Phys. Scr.* **T138** 14048
- [31] Ueda Y., Fukumoto M., Yoshida J., Ohtsuka Y., Akiyoshi R., Iwakiri H. and Yoshida N. 2009 *J. Nucl. Mater.* **386–388** 725–8
- [32] Zhou H.-B., Liu Y.-L., Jin S., Zhang Y., Luo G.-N. and Lu G.-H. 2010 *Nucl. Fusion* **50** 115010
- [33] Tamura T., Kobayashi R., Ogata S. and Ito A.M. 2014 *Model. Simul. Mater. Sci. Eng.* **22** 15002
- [34] Liu Y.-L., Zhang Y., Zhou H.-B., Lu G.-H., Liu F. and Luo G.-N. 2009 *Phys. Rev. B* **79** 172103
- [35] Alimov V.K., Tyburska-Püschel B., Hatano Y., Roth J., Isobe K., Matsuyama M. and Yamanishi T. 2012 *J. Nucl. Mater.* **420** 370–3
- [36] Eckstein W. 2002 *Calculated Sputtering, Reflection and Range Values IPP-Report 9/132*
- [37] Miyamoto M., Nishijima D., Baldwin M.J., Doerner R.P., Ueda Y., Yasunaga K., Yoshida N. and Ono K. 2011 *J. Nucl. Mater.* **415** S657–60

Captions:

**Table 1.** Ne concentration and surface temperature at the center and the edge of the targets exposed to pure D and D-Ne mixed plasmas. The plasma fluences are constant for all targets. D retention containing both D<sub>2</sub> molecule and HD is listed in the last column.

**Figure 1.** Radial distribution of the electron density (a), electron temperature (b) and surface temperature (c) at the target during plasma exposure. NRA measurement positions (0, 1, 3 and 6 mm) are marked as vertical lines.

**Figure 2.** Setup of skimmer and vacuum system in Magnum-PSI. The RGA is located in the turbo pumping line.

**Figure 3.** Neon ion fraction measured by RGA and OES in plasma exposures with different neon gas flow fraction.

**Figure 4.** Surface morphology by SEM of targets exposed to (a) pure D, (b) D-5Ne, (c) D-10Ne and (d) D-20Ne plasma. The images were taken in two magnifications with a higher magnification in the second row.

**Figure 5.** Surface morphology by SEM of a blank target (a) and a target exposed to pure Ne plasma with an incident energy of 40 eV at 553 K and  $5.2 \times 10^{25} \text{ m}^{-2}$  at a low (b) and high magnification (c).

**Figure 6.** SEM images of cross-sections of W targets. In the first row (Top surface), black dashed lines indicate the position of FIB cross-sections. In the second row (Cross-section at low magnifications), white dotted-rectangles labelled by Region A and Region B indicate the location of images taken at high magnifications. In the last row, inter-granular cavity (black dotted rectangle), intra-granular cracks (white rectangles) and (white dotted rectangle) are shown. In D-10Ne and D-20Ne a Pt-C film was deposited onto the investigated surface, featuring as a dark region above W surface.

**Figure 7.** D depth profile of W targets exposed to pure D and D-Ne mixed plasmas. Profile within a depth of 1  $\mu\text{m}$  is amplified and being present in the upper right corner in each case.

**Figure 8.** TDS D<sub>2</sub> desorption profile of W targets exposed to pure D and D-Ne mixed plasmas. The targets were heated up to 1400 K with a linear heating rate of 1 K/s.

**Figure 9.** Surface morphology of W exposed to D-20Ne before (a) and after (b) FIB cutting. The dashed line in (a) indicated the cutting position. The Pt-C protection film is visible in (b).

**Table 1.**

Target	Ne ion concentration	$T_{\text{center}}$ (K)	$T_{\text{edge}}$ (K)	D retention by TDS ( $\text{m}^{-2}$ )
Pure D	0%	550	540	$1.85 \times 10^{21}$
D-5Ne	5%	550	540	$1.34 \times 10^{21}$
D-10Ne	10%	570	530	$6.58 \times 10^{20}$
D-20Ne	20%	540	490	$4.75 \times 10^{20}$

**Figure 1.**

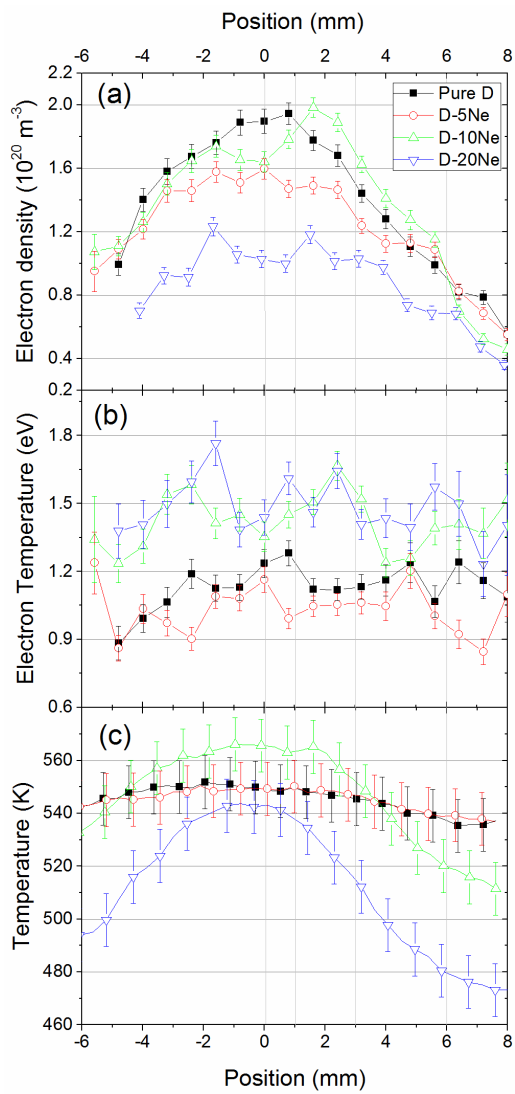


Figure 2.

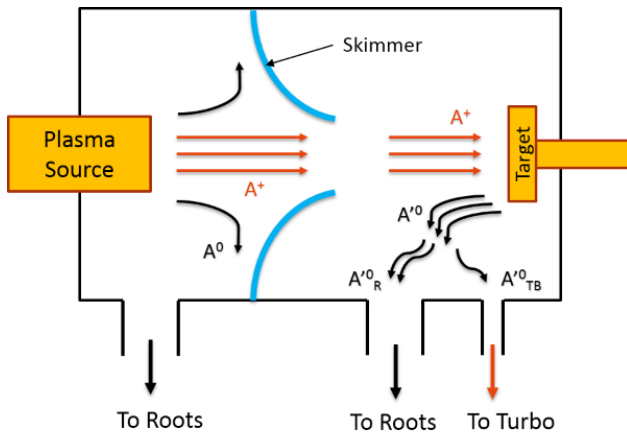
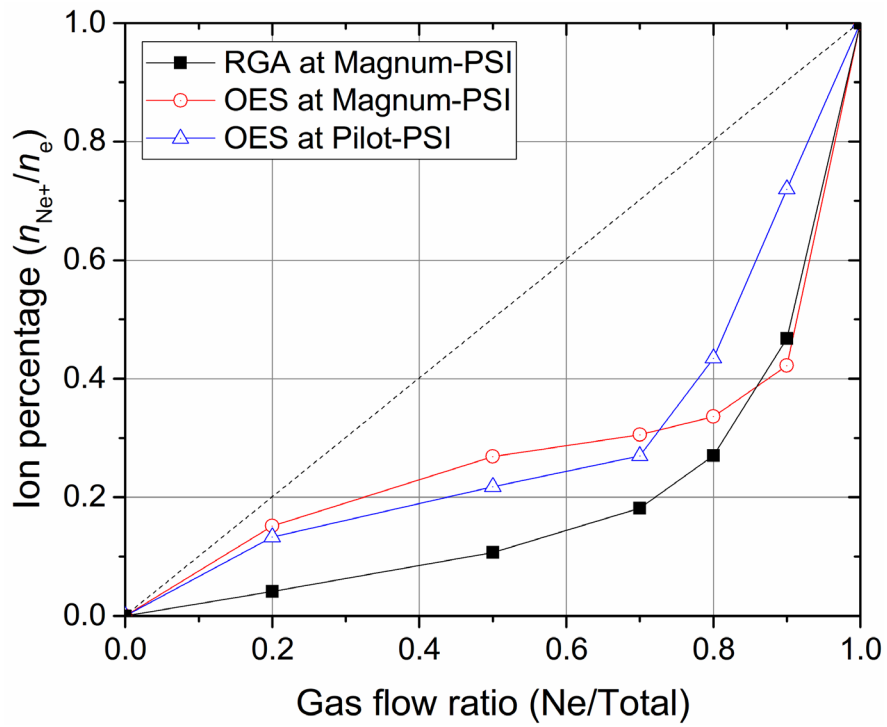
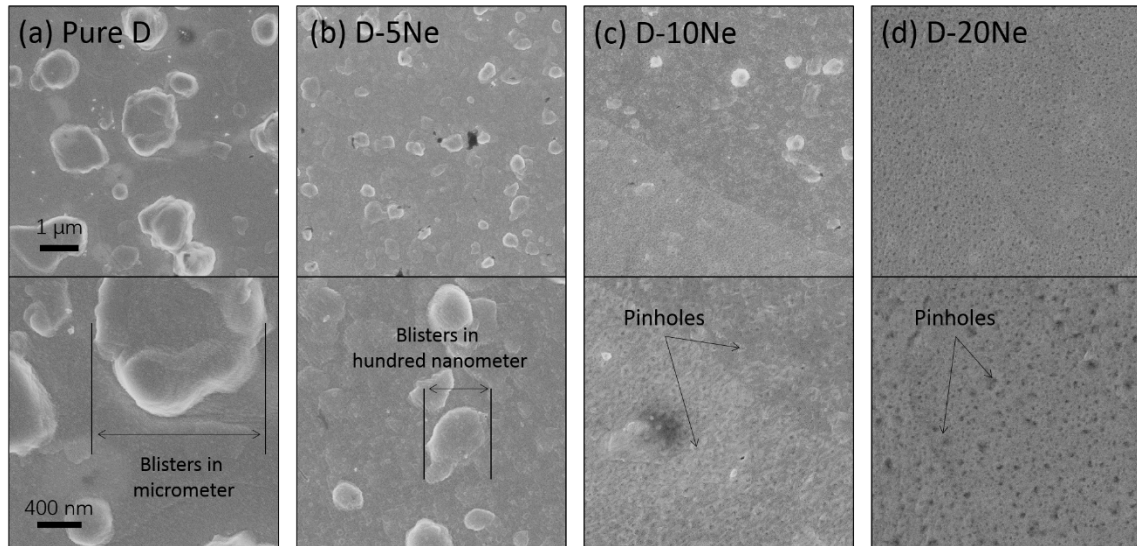


Figure 3.



**Figure 4.**



**Figure 5.**

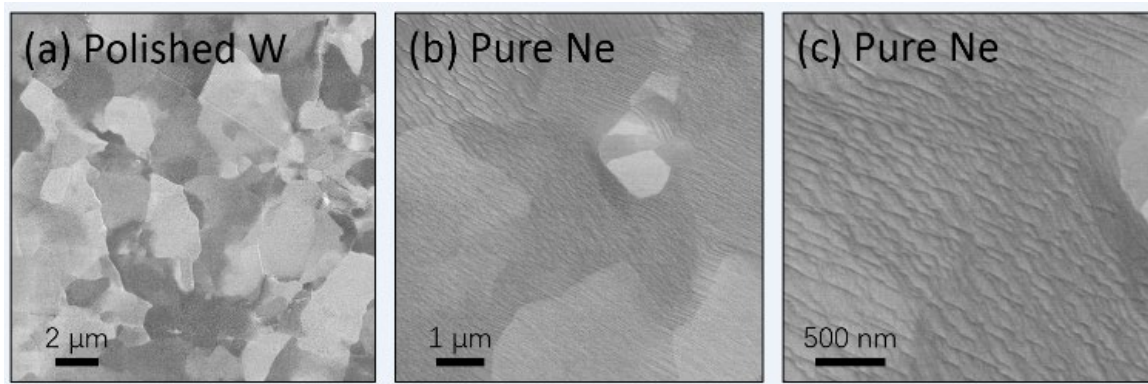


Figure 6.

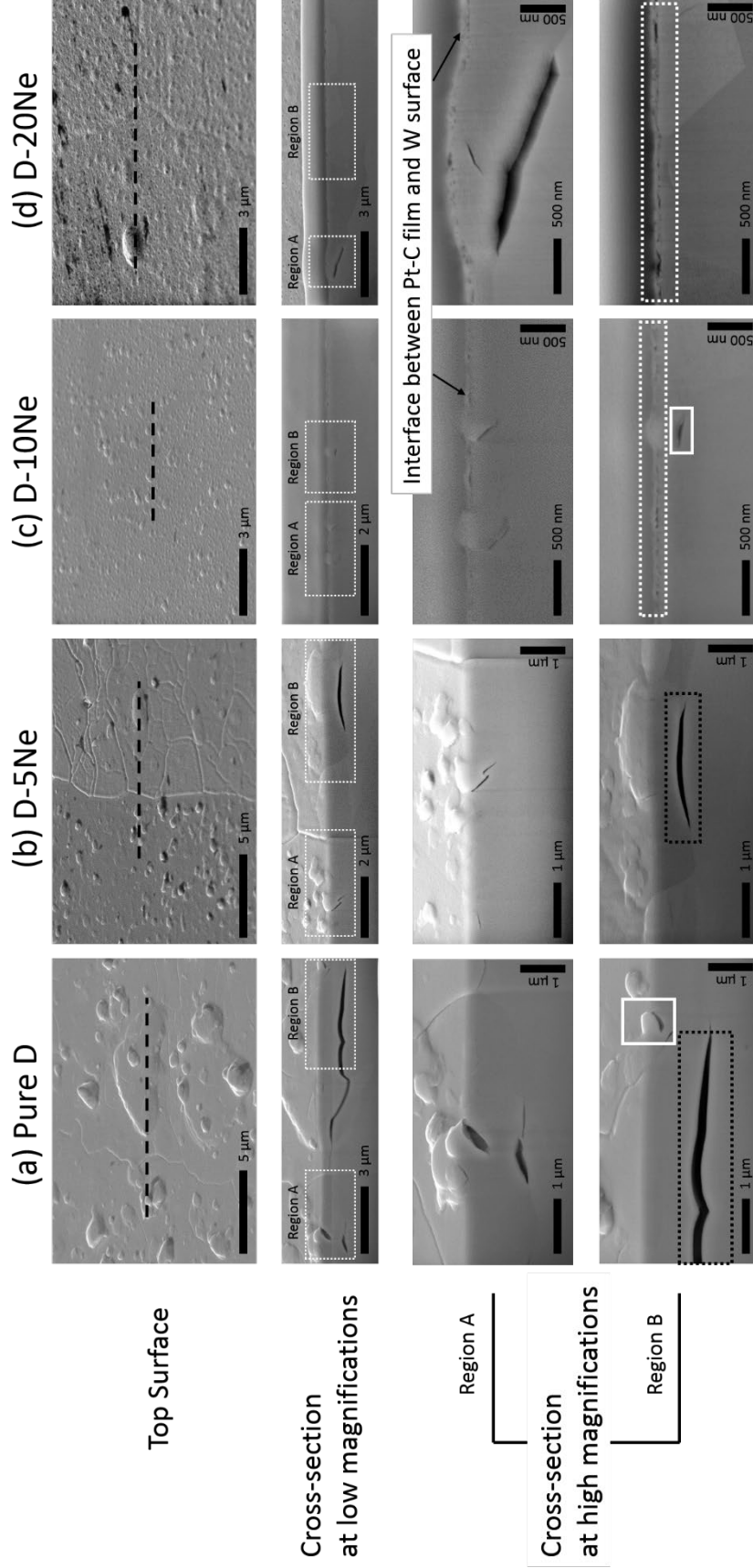


Figure 7.

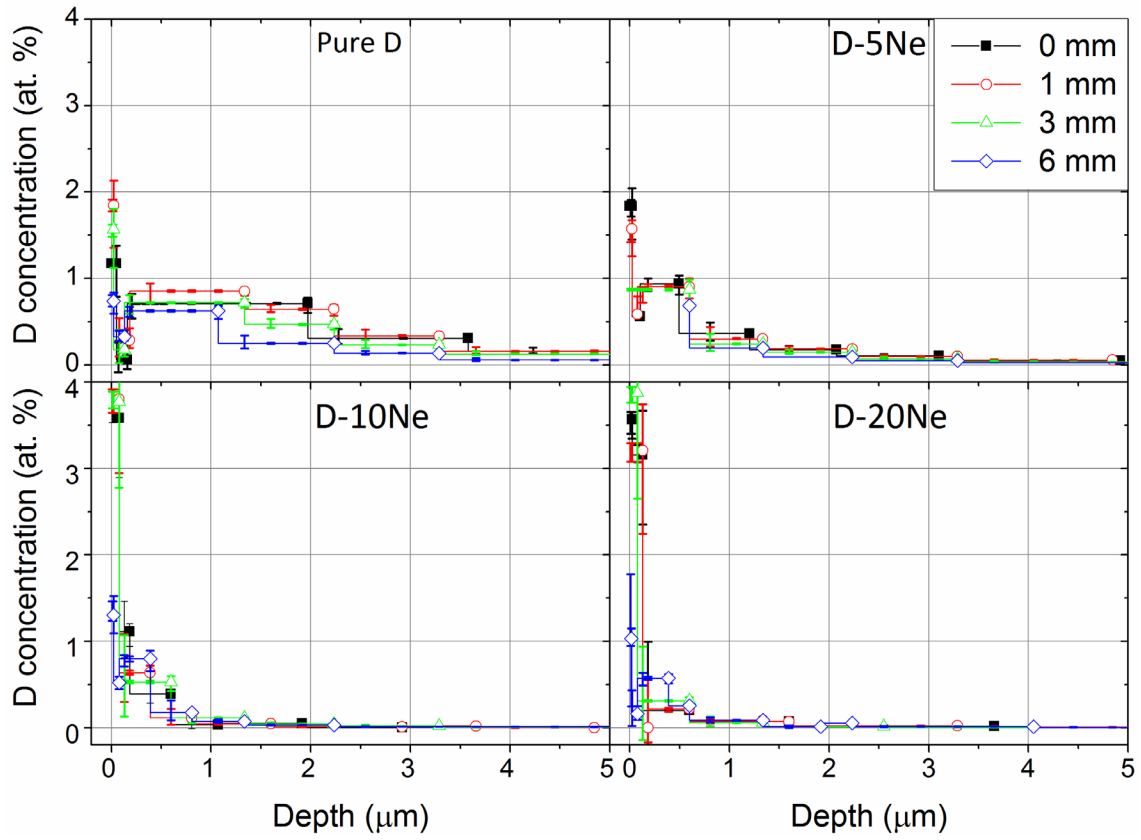


Figure 8.

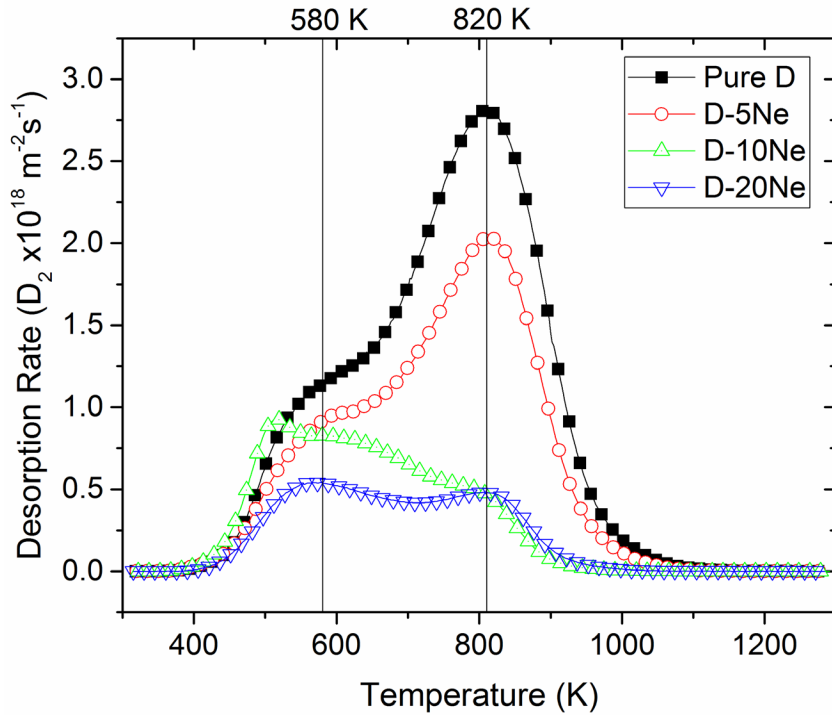




Figure 9.

